

MSDE

Molecular Systems Design & Engineering

rsc.li/molecular-engineering



ISSN 2058-9689

PAPER

Philip D. Howes, Andrew J. deMello *et al.*
Automated microfluidic screening of ligand interactions
during the synthesis of cesium lead bromide nanocrystals



Cite this: *Mol. Syst. Des. Eng.*, 2020, 5, 1118

Automated microfluidic screening of ligand interactions during the synthesis of cesium lead bromide nanocrystals†

Shangkun Li,^a Robert W. Baker,^b Ioannis Lignos,^{‡a} Zhibo Yang,^{§a} Stavros Stavrakis,^{‡a} Philip D. Howes^{‡a} and Andrew J. deMello^{‡a}

Varying the nature of the molecular surface ligands used to synthesize and stabilize lead halide perovskite nanocrystals provides a facile way of tuning and optimizing particle properties. However, the inherently complex reaction parameter space associated with perovskite nanocrystal synthesis complicates this, necessitating long-term and laborious experimentation to optimize conditions for a specific ligand set, and to compare nanoparticle properties across different ligand sets. In the current work, we present an automated microfluidic-based strategy for multidimensional parameter screening, seeking to maximize luminescence intensities and minimize emission bandwidths from quantum confined nanostructures, by monitoring variations in photoluminescence as a function of reaction temperature, base-to-acid ligand ratio, and ligand alkyl chain structure (linear versus branched). For a linear ligand pair (octylamine and octanoic acid), we find two reaction parameter sets that yield bright and narrow emission from nanosheets emitting at 460 nm (synthesized at 100 °C with a low base: acid ratio, FWHM = 25 nm) and nanowires emitting at 497 nm (synthesized at 140 °C with a high base: acid ratio, FWHM = 17 nm). Introducing branched ligands (2-ethylhexylamine and/or 2-ethylhexanoic acid) induces a red shift in emission and shows that bright and narrow emission can only be obtained from weakly quantum-confined nanostructures, within the reaction conditions studied. This work represents the first use of a rapid automated microfluidic system for the screening of ligand interactions during the synthesis lead halide perovskite nanocrystals.

Received 23rd January 2020,
Accepted 21st February 2020

DOI: 10.1039/d0me00008f

rsc.li/molecular-engineering

Design, System, Application

In this work we employ rapid multidimensional reaction parameter screening in the design optimization of cesium lead bromide nanocrystals, with a focus on how changes in molecular surface ligand structure, base:acid ratio and reaction temperature affect resultant photoluminescence properties of the nanocrystals. The system revolves around the use of an automated droplet microfluidic reactor with integrated photoluminescence collection, which allows rapid progression through a user-defined set of synthesis parameters covering the parameter space of interest. While we apply this to the design optimization of cesium lead bromide nanocrystals in a binary organic amine/acid ligand system, the approach could be used for scanning a wide variety of reaction input and output variables, and shows much promise for application in the discovery and optimization of many different functional nanoparticles compositions and reaction formulations.

1. Introduction

The surface ligands of colloidal nanocrystals are fundamental in defining material properties, including size, shape, crystal

phase, electronic character and colloidal stability.^{1–3} The ability to tune and rationally design nanocrystal properties as a function of surface ligand character requires a deep understanding of their molecular properties, behaviour and interactions, before, during and after the growth of the nanocrystal product. Tools that facilitate more efficient screening and characterization of surface ligands in nanocrystal synthesis are vital in expediting the transfer of these promising materials into target applications, including optoelectronics^{4,5} (photovoltaics, displays, lighting) and biomedicine^{6,7} (diagnostics, therapeutics, imaging).

Interest in lead halide perovskite (LHP) nanocrystals has exploded in the half decade since their first reports,^{8,9} with

^a Institute for Chemical and Bioengineering, Department of Chemistry and Applied Biosciences, ETH Zürich, Vladimir Prelog Weg 1, 8093 Zürich, Switzerland.
E-mail: philip.howes@chem.ethz.ch, andrew.demello@chem.ethz.ch

^b Department of Chemistry, University of Bath, Claverton Down, Bath, UK

† Electronic supplementary information (ESI) available. See DOI: 10.1039/d0me00008f

‡ Current address: Department of Chemical Engineering, Massachusetts Institute of Technology, 77 Massachusetts Avenue, Cambridge, MA 02139, USA.

§ Current address: Department of Chemistry, University of California, Berkeley, California 94720, USA.



It is important to note that large scale screening and mapping of reaction parameter spaces in the synthesis of LHP nanocrystals is hindered by the low throughput of traditional flask-based synthetic approaches.^{23,30,31} In this regard, microfluidic technologies possesses significant advantages when compared to batch syntheses.^{36,37} Indeed, the last decade has seen significant developments in the use of microfluidic reactors for nanocrystal synthesis, with many studies reporting improved reaction control and the rapid production of a wide range of products with tailored chemical and photophysical properties.^{38–42} Of particular current interest are segmented flow microfluidic reactors, where the reaction is split into discrete droplets separated by a continuous carrier phase.⁴³ Such formats confer additional advantages when compared to continuous flow approaches; most prominently rapid mixing (that yields nanocrystals with lower polydispersity) and negligible reactor fouling. Additionally, improved heat and mass transfer provides for unrivalled control over reaction parameters, ensuring excellent product-to-product reproducibility.⁴⁴ A key capability of microfluidic reactors of this kind is the capacity to scan large and multidimensional reaction parameter spaces *via* automated reaction control (of precursor dosing, reaction times and temperature) and *in situ* product characterization (by absorption and emission spectroscopies).⁴⁵ Put simply, such approaches allow for a dramatic increase in the rate of information generation/collection, with a concurrent and dramatic decrease in reagent usage, when compared to standard flask-based synthesis methods.

In regard to the synthesis of LHP nanocrystals in segmented-flow microfluidics, significant developments have recently been reported by us,^{46–51} and Abolhasani.^{52,53} Whilst these studies have been instrumental in revealing the nature of growth kinetics of LHP nanocrystals,^{47,52,54} and of compositional tuning for optical and morphological character,^{46,48,49,53} they have not yet been applied to the study of surface ligand effects during the synthesis of nanocrystals.

Herein, we show how an automated microfluidic reactor with integrated photoluminescence detection can be used to perform detailed parametric scans (temperature *versus* base–acid ratio) for defined ligand sets, and critical comparisons between different ligand sets. We study the model case of how ligand structure affects CsPbBr₃ nanocrystal growth in a binary organic acid/amine ligand system. The four tested ligands all possess eight carbons in the alkyl chain, but one set is branched, and the other linear. By repeating the multidimensional parameter scans under identical conditions but substituting in the different ligands, it is possible to conduct a detailed comparison between different conditions and elucidate the effect of alkyl structure on the resultant nanocrystal properties. To our knowledge, this is the first demonstration of a microfluidic platform able to perform high-throughput screening of ligand activities in nanocrystal synthesis, and serves as an important demonstration of the power of multiparametric scanning in the characterization of ligand effects in nanocrystal systems.

2. Materials & methods

2.1 Materials

Cesium carbonate (Cs₂CO₃, Aldrich, 99.9%), lead bromide (PbBr₂, ABCR, 98%), 1-octadecene (ODE, Sigma-Aldrich, 90%), octanoic acid (Sigma-Aldrich, ≥99%), octylamine (Sigma-Aldrich, 99%), 2-ethylhexanoic acid (TCI, >99%), 2-ethylhexylamine (TCI, >98%) were used as received.

2.2 Preparation of precursor solutions

Cesium precursor: Cs₂CO₃ (51 mg) was loaded into a 20 ml Schlenk flask together with 10 ml of ODE and 0.625 ml of organic acid (octanoic or 2-ethylhexanoic acid), dried for 1 h at 120 °C, and then cooled to room temperature under N₂. For the subsequent microfluidic synthesis, the precursor was loaded into a 10 mL Hamilton glass syringe.

Lead bromide precursor: PbBr₂ (138 mg) was loaded into a 20 ml Schlenk flask along with 10 ml of ODE. The cloudy mixture was heated to 120 °C under vacuum, and then the total 7.5 mmol of ligands (base plus acid at 2 : 1 or 1 : 1 base : acid) were added under a N₂ atmosphere. After the PbBr₂ dissolved completely, the solution was cooled to room temperature under N₂ before being loaded into a 10 ml Hamilton glass syringe.

2.3 Microfluidic synthesis of nanocrystals

The precursor-loaded syringes were positioned on precision syringe pumps (neMESYS, Cetoni GmbH, Germany). Two sy-

ringes were filled with PbBr₂ precursor with different ratios of ligands. One syringe was used to inject the carrier fluid (Galden Fluorinated Fluid, Blaser Swisslube AG, Germany) while another was used to inject Cs precursor. The precursors and oil were all conveyed separately through polytetrafluoroethylene (PTFE) tubing (1/16" OD, 0.5 mm ID, IDEX Health & Science, USA) into a polyether ether ketone (PEEK) 7-port manifold (0.5 mm thru-hole, IDEX Health & Science, USA), where they combined to form a segmented flow. The ratio of carrier phase (oil) to dispersed phase (ODE) could be controlled precisely, along with the exact base–acid ligand ratio within the dispersed phase, by varying the pump rates of the four separate syringes. Droplets were conveyed through the tubing onto a heating module, where the tubing was wrapped around a copper rod heated to a user-defined reaction temperature. After exiting the heating unit, inline fluorescence measurements were performed on droplets using a 365 nm LED light source (M365LP1, Thorlabs, Germany) and a fiber coupled spectrometer (QE 65 Pro, Ocean Optics, USA) for detection, with an integration time of 30 milliseconds. Each parameter set was run for 2 minutes, and data was recorded for the last 30 seconds of this to allow for reactor pressure equilibration. All reactor units are controlled and systematically linked together using an in-house-developed LabVIEW program, which automatically adjusts the temperature, flow rate, and residence time while managing data logging. All photoluminescence spectra were measured inline without any product purification.

2.4 Data analysis

Each experimental run yielded 121 .csv files containing 335 spectra each. These were processed using a custom Python script to average the data in each file, to compile all data, to perform calculations of dominant peak position, median, interquartile range and peak intensity, and to plot all spectra, scatter, and contour plots.

2.5 Offline characterization

Selected reaction products were collected at the exit of the reactor for later analysis by transmission electron microscopy (TEM) (Hitachi HT7700, accelerating voltage 100 kV). TEM samples were prepared using crude products without further processing.

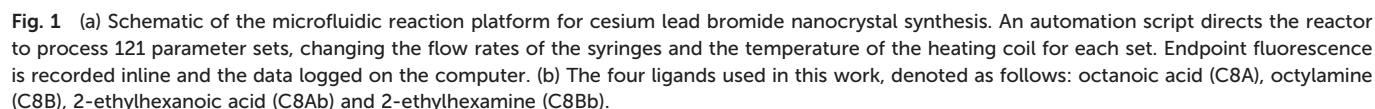
3. Results

General system description

Cesium lead bromide nanocrystals were synthesized following literature protocols,⁵⁴ with some modifications. The cesium, lead and bromine precursors were maintained at a constant concentration (yielding a Cs:Pb:Br ratio of 1:2.9:5.8), whilst the reaction temperature and the ratio between the amine and acid ligands was varied during experiment (between 90 and 190 °C, and a base:acid ratio of 0.7:1 to 1.2:1). Accordingly, changes in photoluminescence and size/



When analysing spectral data, we report the dominant peak position, the median peak position, the peak intensity and the interquartile range (see Fig. S2[†]). The dominant peak



position indicates the dominant emitting species in the reaction solution, but ignores any subpeaks present. The median emission wavelength is used as an indicator of average emission wavelength weighted by intensity (note, although the value itself does not correspond to a specific excited state, for spectra containing only one peak, the value tends towards the peak emission wavelength). The peak intensity is used as a measure of the brightness of the dominant reaction product. It should be noted that we do not compare the peak emission intensities between ligand sets, as excitation intensities vary between experiments. Furthermore, the interquartile range (IQR) is used in preference to the full width at half maximum (FWHM), since many of the spectra contain several convoluted peaks; the IQR yields a single value as an indicator of the spread of emission wavelengths in a sample.

Mapping trends within a single experiment

Multiple input and output variables are used to map the parameter space and to identify the optimal conditions for a given ligand set. Using the linear ligand set C8B–C8A, we sought to find reaction conditions that yield high emission intensities and low spectral widths (or IQRs). Fig. 2 presents extracted data as a series of contour plots (a–c) and spectral series (d–g) extracted along lines of interest in the contour plots. In this way, it is possible to use the contour plots for a broad survey of the reaction parameter space, and then to extract specific spectra of interest for further study. A general shift in the median emission towards the red is observed as a function of reaction temperature, within the range 460 to 500 nm. As the bulk emission of CsPbBr₃ occurs at approximately



Fig. 2 Screening results for the linear ligand set C8B–C8A. The contour plots show (a) median emission, (b) interquartile range and (c) peak intensity as a function of base:acid ratio and temperature. The white dashed lines in the contour plots correspond to the four spectral series shown in panels (d–g).



525 nm (well above the indicated range), we see that all nanostructures synthesized in this parameter space are quantum confined.⁵⁸ There is a smaller dependence of the median emission on base:acid ratio. The distinct spectral peaks do not shift continuously, but instead rise or fall within relatively narrow ranges (Fig. 2d–g), suggesting the presence of several distinct species. There is a clear relationship between input variables and peak intensity, with two distinct regions of high intensity being visible in Fig. 2c and occurring at approxi-

mately 110 °C and 140 °C. At 110 °C, a lower base:acid ratio yields a higher peak intensity, whereas at 140 °C a higher base:acid ratio yields a higher peak intensity. There is clear relationship between the “valley” separating these high intensity regions and the region where the IQR reaches a maximum, as emission is shared between two distinct species emitting at 460 or 497 nm in the intermediate zone. Accordingly, the maximum intensity is less than in neighbouring regions, where emission is dominated by single emitting

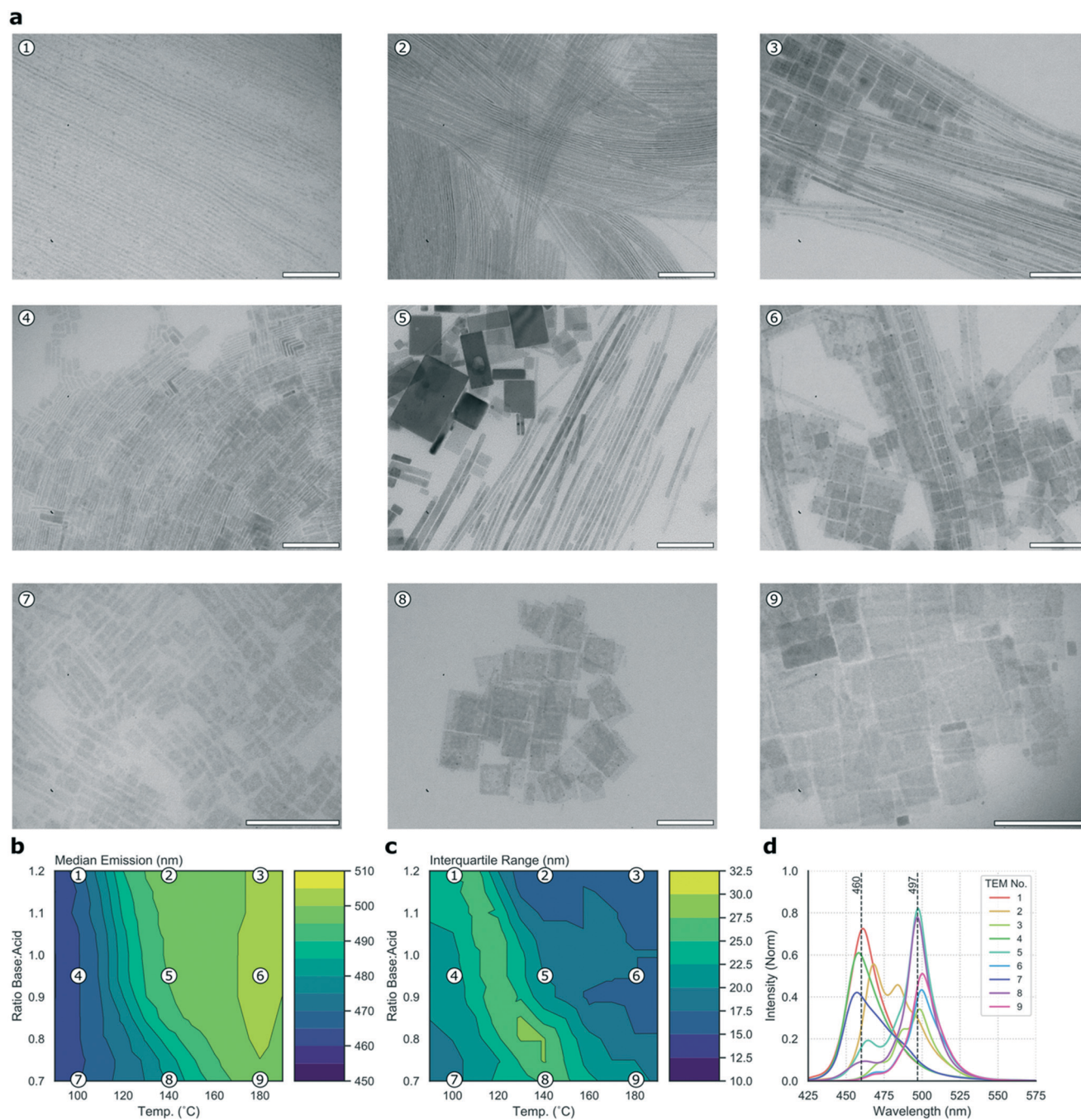


Fig. 3 (a) TEM micrographs of nine samples taken from the C8B–C8A experiment. Scale bar = 100 nm. (b and c) Contour maps of the sampling points in the median emission and interquartile range contour plots. (d) The emission spectra associated with the nine samples marked.



To cast further light on the large data set collected during the high-throughput microfluidic experiments, it is possible to collect a subset of samples for detailed offline analysis. Fig. 3a presents nine TEM micrographs of samples collected for the C8B–C8A experiment, sampled from points dispersed equidistantly through the parameter space and mapped in relation to the median and IQR contour plots in Fig. 3b and c, respectively, with the corresponding emission spectra shown in Fig. 3d. It should be noted that TEM imaging can be problematic for LHP nanocrystals, as the high energy electron beam can degrade samples.⁵⁹ Further, studying the crude reaction product means that there are often many different structures visible in the micrographs (*e.g.* Fig. 3a5). These two issues make quantitative assessment of the different populations challenging, however the images do provide an indication of types of morphologies present, which can be related to the experimental data. In the current study, micrographs revealed two distinct species—nanoplates and nanowires, albeit with widely ranging dimensions. High base:acid ratios appear to favour nanowire formation, with products tending towards nanosheets at higher temperatures and lower base:acid ratios, an observation that is in agreement with previous results.^{22,60} Fig. 3 shows that the two highly emissive species highlighted above correspond to nanowires emitting at 497 nm (synthesized at 140 °C with high base:acid ratio) and nanosheets emitting at 460 nm (synthesized at 100 °C with low base:acid ratio). Although products synthesized at 110 °C with low base:acid ratio exhibit slightly higher emission intensities, this is at the expense of a higher IQR, so we suggest that the 100 °C condition offers a better overall result. Fig. S3a† shows the position of the two species within the parameter space, and their full emission spectra. Nanoplates emitting at 460 nm have a full width at half maximum (FWHM) of 25 nm, while nanowires emitting at 497 nm have a FWHM of 17 nm. Previous studies of CsPbBr₃ nanocrystals have revealed a strong correlation between the thickness of nanostructures (in terms of crystalline unit cells) and the emission wavelength, due to quantum confinement of excitons.⁹ Bulk emission occurs at approximately 2.36 eV (525 nm), with higher energy emission occurring in the quantum confinement regime with nanostructures below the excitonic Bohr diameter (which is 7 nm for CsPbBr₃).^{9,58} As the two major peaks in the spectral series of the linear ligands experiment occur at 460 and 497 nm, they can be ascribed to quantum-confined structures of CsPbBr₃. The 460 and 497 nm peaks map to nanostructures of 3 and 11 unit cells, respectively.^{58,61} In summary, this experiment demonstrates how simultaneously scanning several input variables, and studying several output variables in concert allows ready visualization and selection of optimal reaction conditions, here revealing two distinct regions of useful emission characteristics from quantum confined nanostructures.

The remaining two ligand sets (C8B–C8Ab and C8Bb–C8Ab) showed less variation in emission character within each experiment, so they are now reviewed only briefly. For the C8B–C8Ab ligand set, we observe a dependence of median emission and IQR on temperature, with spectra red-shifting and narrowing with increasing temperature; but less of a dependence on the base:acid ratio (Fig. S5a and b†). However, as shown in Fig. S5c,† the peak fluorescence intensity does show a dependence on base:acid ratio, with a lower ratio favouring higher intensities, and a maximum occurring at high temperatures and low base:acid ratios. Inspection of the three contour plots together indicates that there is a region that yields products in the weak quantum confinement regime (emission between 500 and 525 nm), with relatively bright and narrow emission, corresponding to the center and lower left portions of the parameter space as plotted. Within this region, bright and narrow quantum-confined emission is observed along the base:acid ratio 0.7 line (Fig. S5f†), below a temperature of 140 °C (Fig. S5e†). Fig. S3c† shows the position of three products in this region of parameter space, and their full emission spectra. The TEM map shown in Fig. S6† exhibits a variety of nanostructures, including nanosheets

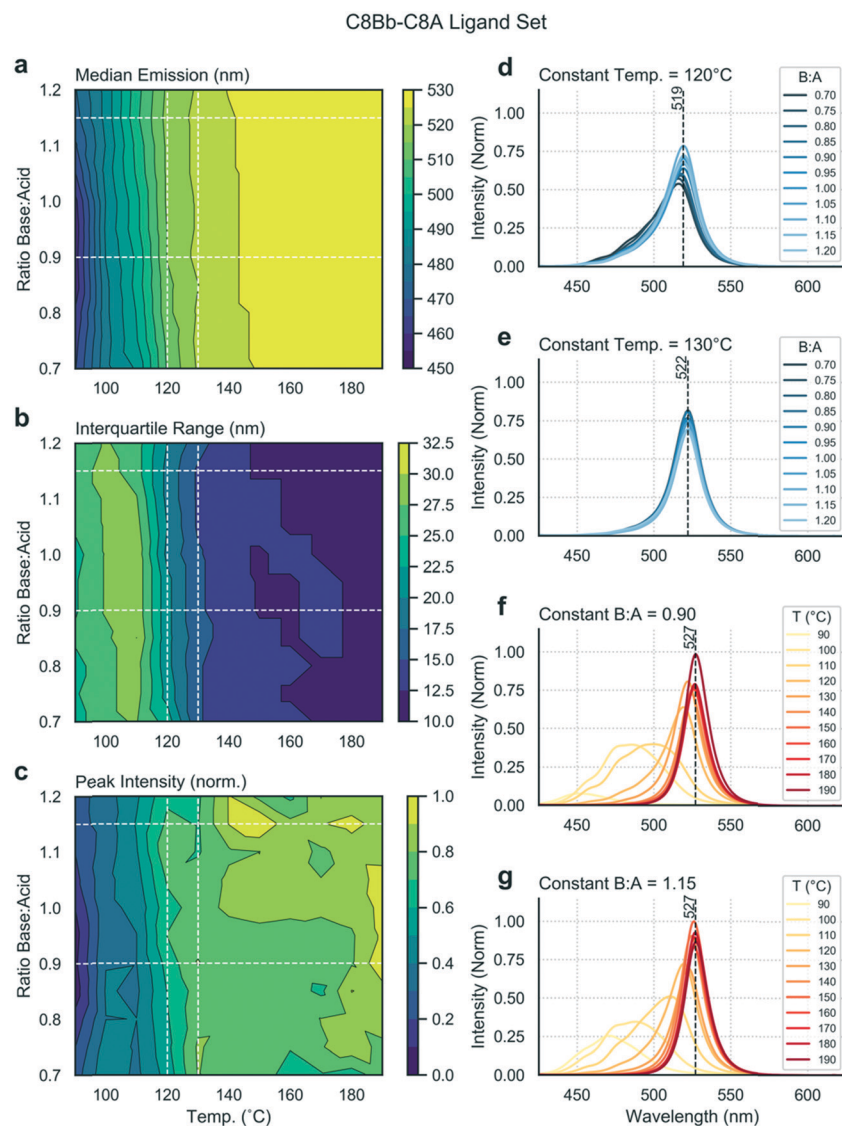


Fig. 4 Screening results for the ligand set C8Bb-C8A. The contour plots show (a) median emission, (b) interquartile range and (c) peak intensity as a function of base:acid ratio and temperature. The white dashed lines in the contour plots correspond to the four spectral series shown in panels (d-g).

with large lateral dimensions, similar to those synthesized by Shamsi *et al.* using a mixed C_8/C_{18} binary ligand system.²⁵ Further, under reaction conditions of 140 °C and base:acid ratio of 0.95, nanocubes are obtained with an emission peak in weak confinement, at 515 nm.

Finally, Fig. S7† presents a detailed analysis of the C8Bb-C8Ab ligand set, where all of the reaction products yield peaks above 519 nm, with low IQR in all cases. However, the peak intensity does vary considerably across the data set. There is a narrow temperature range (between 90 and 100 °C) that yields emission peaks at approximately 520 nm, with maximum intensity occurring at 0.95 base:acid ratio at 100 °C. Fig. S3d† shows the position of four products in this region of the parameter space, with their full emission spectra. Emission at 520 nm suggests very weak quantum confinement. Fig. S8†

shows the TEM map for the branched ligand set, exhibiting a mixture of nanocubes and nanospheres, and some larger aggregates.

Mapping trends between experiments

Using the methodology outlined herein, it is possible to make detailed comparisons between experiments and elucidate the effects of different ligands on the reaction output variables. To compare the data sets for the four ligand combinations studied in this work, the contour plots were directly compared (Fig. 5a and c) and data extracted to visualize the differing effects between the ligand sets (Fig. 5b and d). Fig. 5a contrasts the median emission wavelength contour plots for the four ligand sets, while Fig. 5b shows two scatter plots with data series extracted at a constant base:acid ratio



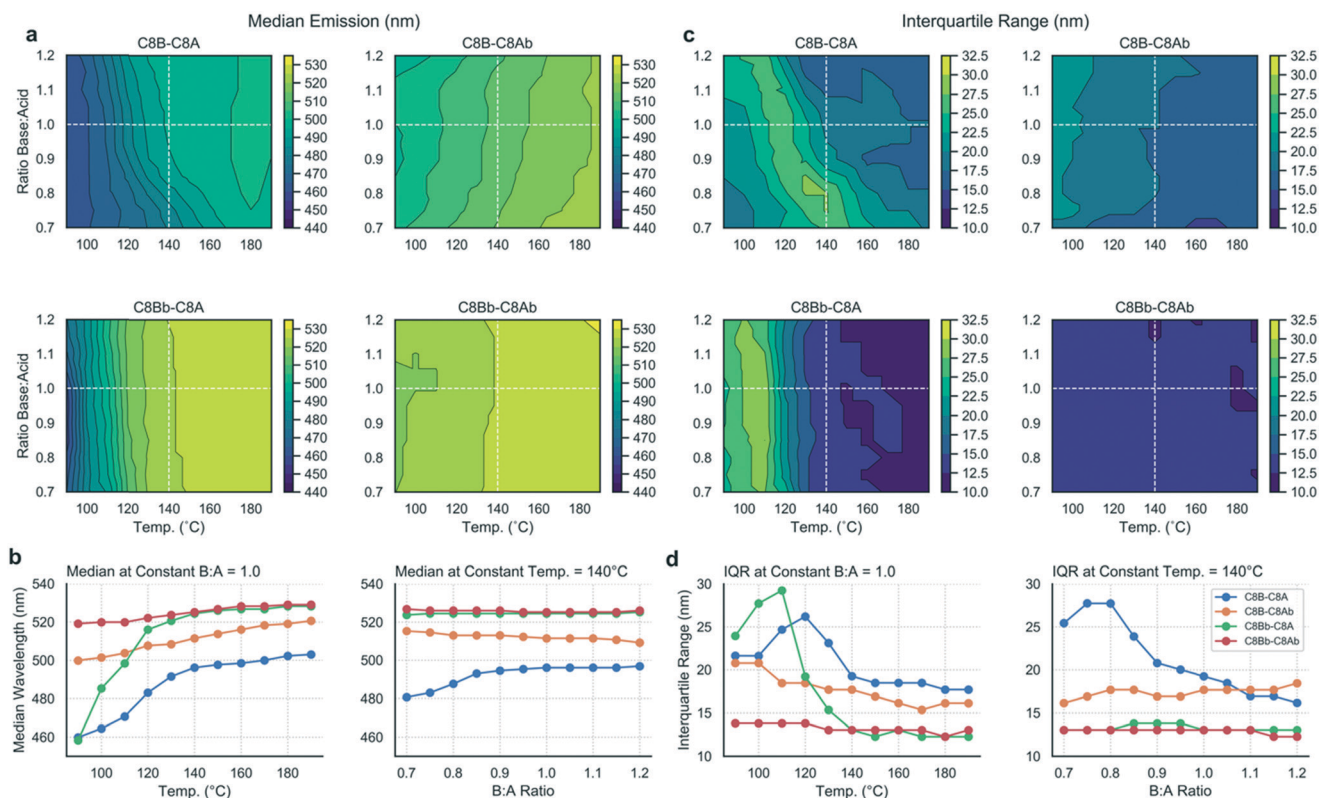


Fig. 5 Comparison between the four ligand sets. (a) The median emission contour plots, plotted with the same colour scale. (b) Scatter plots comparing the median emission wavelengths of the four ligand sets at a constant base:acid ratio (1.0) and a constant temperature (140 °C). (c) The interquartile range contour plots, plotted against the same colour range. (d) Scatter plots comparing the interquartile ranges of the four ligand sets at a constant base:acid ratio (1.0) and a constant temperature (140 °C). The dashed white lines on the contour plots correspond to the series extracted for the scatter plots.

(1.0), and a constant temperature (140 °C), corresponding to the dashed white lines on the contour plots and chosen as instructive lines of comparison.

From the median emission contour plots, we can see that the C8Bb-C8Ab ligand set (*i.e.* both branched ligands) yields the most consistent result across the data set, with no dependence on base:acid ratio and little temperature dependence, which is shown in the corresponding scatter plots in Fig. 5b (red line). In contrast, the C8B-C8A ligand set (*i.e.* where both ligands are linear) shows a dependency on both base content and temperature. The C8Bb-C8A set shows the biggest shift in emission, as a function of temperature, but no dependence on base:acid ratio (green line). For the IQR contour plots (Fig. 5c), again the biggest contrast is between the C8B-C8A and C8Bb-C8Ab data sets, with the branched ligands showing constant IQR in all conditions, but the linear ligands allowing a large range of IQRs reflective of the varied reaction products as discussed above. The most striking shift in IQR is seen for the C8Bb-C8A as a function of temperature (Fig. 5d), with the C8B-C8A set also showing a pronounced reduction with increasing temperature. Overall, the scatter plots indicate that changing the temperature has a more pronounced effect on the median and IQR than changing the base:acid ratio.

4. Discussion

In this work we have demonstrated how a microfluidic platform can be used to investigate the effect of input variables, including ligand structure, ligand base–acid ratio and temperature, on the nature of the reaction products in the synthesis of cesium lead bromide nanocrystals, with a view to accelerating the search for reaction conditions that yield bright and narrow emission from quantum confined nanostructures. We have observed a variety of nanostructures, predominantly nanosheets and nanowires. Such anisotropic growth of CsPbBr₃ nanocrystals is common with alkylammonium ligands as they preferentially bind to the basal plane of the structure, restricting growth in the vertical axis and more readily permitting lateral growth.⁶² Further, reaction solutions rich in aliphatic ammonium ions encourage anisotropic growth due to competition between the RNH₃⁺ and Cs⁺ ions.²²

Additionally, we have observed that, in the case of the linear ligand set C8B-C8A, there are two distinct regions in the reaction parameter space that yield high intensity emission and low emission width. The regions correspond to distinct products emitting at two different wavelengths, both in the quantum confined regime (*i.e.* dimensional confinement below the exciton Bohr diameter of 7 nm for CsPbBr₃). Synthesis at 100 °C with lower base:acid ratio yields nanosheets with



Although introducing branched ligands can offer a steric effect to hinder monomer diffusion, our studies demonstrate the opposite effect, yielding larger nanostructures with more red-shifted emission. We suggest that the disruptive effect of the branched ligands on ligand packing dominates over steric hindrance of monomer diffusion, allowing increased monomer addition, increased growth rates and larger final structures. This is likely a consequence of the short alkyl chain lengths used in this study. Interestingly, introducing the branched acid (C8B–C8Ab) yielded a greater red shift with fewer blue emitting species compared to introducing the branched amine (C8Bb–C8A). This is somewhat counterintuitive given the common presumption that the dominant surface ligand is alkylammonium. However, several studies have suggested that carboxylic acid and carboxylate ligands are in fact present in significant amounts on the surface of CsPbBr₃ nanocrystals,^{20,21,23} with the amine and carboxylic acids showing facet-dependent binding.³⁰ Further, the multiple states and roles of each ligand before, during and after the reaction,^{21,65} make this effect hard to disentangle in the context of the current study. However, we note that the effects of ligand branching are evidently not restricted to sterics, but

It is also important to note that a limitation of fluorescence spectra is that little information can be discerned for nanoparticles above the quantum confinement regime (7 nm here, with emission around 525 nm), as changes in size and shape do not yield changes in emission, therefore structural characteristics outside the quantum confinement regime cannot be discerned. Accordingly, it would be highly beneficial to include also inline absorption spectroscopy in future studies, as such analyses reveal additional information, for

example on crystal structure, which are not discernible from the photoluminescence spectra alone. An important reaction variable that was not studied in the current work, but could readily be integrated, is the reaction time. For example, it was previously shown that by extending the reaction time under the conditions previously used for CsPbBr₃ nanocube synthesis, nanowires with diameters below 12 nm and lengths up to 5 μm were obtained.⁶⁷ It is evident that the more the reaction parameter space can be expanded (including further input variables and output variables), the more powerful this data driven approach to product optimization will be. This will be the focus of future work.

We note that there are some mechanistic differences in how the synthesis of LHP nanocrystals proceeds in our microreactor as opposed to the flask-based approach. Following the hot-injection approach developed by Kovalenko and co-workers,⁹ CsPbX₃ nanocrystals form after the injection of a Cs-oleate solution into a hot octadecene solution of PbX₂ (from 140–200 °C), followed by rapid quenching in an ice bath after five seconds. In contrast, in our microfluidic reactor precursors are mixed at room temperature in a microfluidic manifold, and then conveyed to a rod which heats the reaction solution to the desired reaction temperature (90–190 °C herein), with a residence time of 30 seconds before cooling to room temperature. Despite these differences, our previous studies have demonstrated excellent agreement in results obtained using equivalent reaction conditions in the microfluidic and bulk approaches.⁴⁶ This is an important observation, as it makes comparisons between literature data using the hot-injection approach and our microfluidic data meaningful. However, it should not be forgotten that the microfluidic approach has inherent advantages (such as rapid mixing and heat transfer leading to lower polydispersity,³⁷ excellent batch-to-batch reproducibility³⁶ and potential for industrial scale-up⁶⁸) that mark it as a desirable synthesis methodology in itself, and not solely as a means of performing high-throughput screening.

5. Conclusions

Herein, we have demonstrated how an automated microfluidic reactor with *in situ* photoluminescence characterisation can be used to map a two dimensional parameter space (scanning base:acid ligand ratio and reaction temperature), in search of reaction conditions that yield quantum confined nanostructures with bright and narrow emission properties. Our results demonstrate the time and material efficiency of automated multidimensional parameter screening *versus* a one-factor-at-a-time optimization approach normally undertaken in conventional synthesis routes.

We feel this approach shows potential for impact in some areas of study that are pertinent to the advancement of the LHP nanocrystal field. First, it is desirable to discover and employ reaction conditions that yield inherently low polydispersity, rather than relying on *post hoc* product purification to isolate specific products, which is both involved and ineffi-

cient. We have demonstrated this by identifying two reaction parameters sets in the C8B–C8A experiment that both yield bright and narrow emission. Second, it is evident from the literature that the binary organic amine–acid ligand system has some disadvantages (*e.g.* poor surface binding²⁰) that inherently limit the product stability. Our study herein has demonstrated the complexity of the parameter space for even a relatively simple binary ligand system, with a strong dependence on reaction temperature and ligand ratio. The discovery and optimization of new ligands, and formulations in multinary ligands systems, will likely require such advanced experimental approaches to aid new discoveries. Third, as we enter a data-driven era of nanomaterials discovery and optimization,^{55,69} we feel approaches such as the one presented herein may yield extraordinary gains when combined with advanced tools such as machine learning and directed evolution.^{70–72}

Conflicts of interest

The authors have no conflicts of interest to declare.

Acknowledgements

S. L. would like to thank Richard Maceiczky and Leonard Bezing for kind advice in using and developing the microfluidic platform. P. D. H. and S. S. would like to thank the Swiss National Science Foundation (SNSF) for support *via* a Spark Grant (Project No. CRSK-2_190750). The authors are grateful to the ScopeM center at ETH for technical assistance in TEM imaging. Finally, the authors would like to thank Kane Shenton for help in developing the Python scripts used in this work.

References

- 1 M. A. Boles, D. Ling, T. Hyeon and D. V. Talapin, *Nat. Mater.*, 2016, **15**, 141–153.
- 2 A. Heuer-Jungemann, N. Feliu, I. Bakaimi, M. Hamaly, A. Alkilany, I. Chakraborty, A. Masood, M. F. Casula, A. Kostopoulou, E. Oh, K. Susumu, M. H. Stewart, I. L. Medintz, E. Stratakis, W. J. Parak and A. G. Kanaras, *Chem. Rev.*, 2019, **119**, 4819–4880.
- 3 S. Lazzari, P. M. Theiler, Y. Shen, C. W. Coley, A. Stemmer and K. F. Jensen, *Langmuir*, 2018, **34**, 3307–3315.
- 4 S. V. Kershaw, L. Jing, X. Huang, M. Gao and A. L. Rogach, *Mater. Horiz.*, 2017, **4**, 155–205.
- 5 Y. Fu, H. Zhu, J. Chen, M. P. Hautzinger, X.-Y. Zhu and S. Jin, *Nat. Rev. Mater.*, 2019, **4**, 169–188.
- 6 H. Kim, S. Beack, S. Han, M. Shin, T. Lee, Y. Park, K. S. Kim, A. K. Yetisen, S. H. Yun, W. Kwon and S. K. Hahn, *Adv. Mater.*, 2018, **30**, 1701460.
- 7 D. Kim, K. Shin, S. G. Kwon and T. Hyeon, *Adv. Mater.*, 2018, **30**, 1802309.
- 8 L. C. Schmidt, A. Pertegás, S. González-Carrero, O. Malinkiewicz, S. Agouram, G. Mínguez Espallargas, H. J. Bolink, R. E. Galian and J. Pérez-Prieto, *J. Am. Chem. Soc.*, 2014, **136**, 850–853.



- 9 L. Protesescu, S. Yakunin, M. I. Bodnarchuk, F. Krieg, R. Caputo, C. H. Hendon, R. X. Yang, A. Walsh and M. V. Kovalenko, *Nano Lett.*, 2015, **15**, 3692–3696.
- 10 Q. A. Akkerman, G. Rainò, M. V. Kovalenko and L. Manna, *Nat. Mater.*, 2018, **17**, 394–405.
- 11 D. Aldakov and P. Reiss, *J. Phys. Chem. C*, 2019, **123**, 12527–12541.
- 12 J. Shamsi, A. S. Urban, M. Imran, L. De Trizio and L. Manna, *Chem. Rev.*, 2019, **119**, 3296–3348.
- 13 D. H. Fabini, J. G. Labram, A. J. Lehner, J. S. Bechtel, H. A. Evans, A. Van der Ven, F. Wudl, M. L. Chabinye and R. Seshadri, *Inorg. Chem.*, 2017, **56**, 11–25.
- 14 H. Fu, *J. Mater. Chem. A*, 2019, **7**, 14357–14379.
- 15 D. Yang, X. Li and H. Zeng, *Adv. Mater. Interfaces*, 2018, **5**, 1701662.
- 16 J. Yin, G. H. Ahmed, O. M. Bakr, J.-L. Brédas and O. F. Mohammed, *ACS Energy Lett.*, 2019, **4**, 789–795.
- 17 M. Gong, R. Sakidja, R. Goul, D. Ewing, M. Casper, A. Stramel, A. Elliot and J. Z. Wu, *ACS Nano*, 2019, **13**, 1772–1783.
- 18 B. Luo, S. B. Naghadeh and J. Z. Zhang, *ChemNanoMat*, 2017, **3**, 456–465.
- 19 T. A. Berhe, W.-N. Su, C.-H. Chen, C.-J. Pan, J.-H. Cheng, H.-M. Chen, M.-C. Tsai, L.-Y. Chen, A. A. Dubale and B.-J. Hwang, *Energy Environ. Sci.*, 2016, **9**, 323–356.
- 20 J. De Roo, M. Ibáñez, P. Geiregat, G. Nedelcu, W. Walravens, J. Maes, J. C. Martins, I. Van Driessche, M. V. Kovalenko and Z. Hens, *ACS Nano*, 2016, **10**, 2071–2081.
- 21 R. Grisorio, M. E. Di Clemente, E. Fanizza, I. Allegretta, D. Altamura, M. Striccoli, R. Terzano, C. Giannini, M. Irimia-Vladu and G. P. Suranna, *Nanoscale*, 2019, **11**, 986–999.
- 22 G. Almeida, L. Goldoni, Q. Akkerman, Z. Dang, A. H. Khan, S. Marras, I. Moreels and L. Manna, *ACS Nano*, 2018, **12**, 1704–1711.
- 23 A. Pan, B. He, X. Fan, Z. Liu, J. J. Urban, A. P. Alivisatos, L. He and Y. Liu, *ACS Nano*, 2016, **10**, 7943–7954.
- 24 K. Chen, Q. Zhong, W. Chen, B. Sang, Y. Wang, T. Yang, Y. Liu, Y. Zhang and H. Zhang, *Adv. Funct. Mater.*, 2019, **29**, 1900991.
- 25 J. Shamsi, Z. Dang, P. Bianchini, C. Canale, F. Di Stasio, R. Brescia, M. Prato and L. Manna, *J. Am. Chem. Soc.*, 2016, **138**, 7240–7243.
- 26 C. B. Murray, D. J. Norris and M. G. Bawendi, *J. Am. Chem. Soc.*, 1993, **115**, 8706–8715.
- 27 B. Luo, Y.-C. Pu, S. A. Lindley, Y. Yang, L. Lu, Y. Li, X. Li and J. Z. Zhang, *Angew. Chem., Int. Ed.*, 2016, **55**, 8864–8868.
- 28 H. Huang, B. Chen, Z. Wang, T. F. Hung, A. S. Susha, H. Zhong and A. L. Rogach, *Chem. Sci.*, 2016, **7**, 5699–5703.
- 29 D. Yan, T. Shi, Z. Zang, T. Zhou, Z. Liu, Z. Zhang, J. Du, Y. Leng and X. Tang, *Small*, 2019, **15**, 1901173.
- 30 S. Sun, D. Yuan, Y. Xu, A. Wang and Z. Deng, *ACS Nano*, 2016, **10**, 3648–3657.
- 31 Z. Liang, S. Zhao, Z. Xu, B. Qiao, P. Song, D. Gao and X. Xu, *ACS Appl. Mater. Interfaces*, 2016, **8**, 28824–28830.
- 32 F. Krieg, Q. K. Ong, M. Burian, G. Rainò, D. Naumenko, H. Amenitsch, A. Süess, M. J. Grotevent, F. Krumeich, M. I. Bodnarchuk, I. Shorubalko, F. Stellacci and M. V. Kovalenko, *J. Am. Chem. Soc.*, 2019, **141**, 19839–19849.
- 33 F. Krieg, S. T. Ochsenbein, S. Yakunin, S. ten Brinck, P. Aellen, A. Süess, B. Clerc, D. Guggisberg, O. Nazarenko, Y. Shynkarenko, S. Kumar, C.-J. Shih, I. Infante and M. V. Kovalenko, *ACS Energy Lett.*, 2018, **3**, 641–646.
- 34 Y. Yang, H. Qin and X. Peng, *Nano Lett.*, 2016, **16**, 2127–2132.
- 35 Y. Yang, H. Qin, M. Jiang, L. Lin, T. Fu, X. Dai, Z. Zhang, Y. Niu, H. Cao, Y. Jin, F. Zhao and X. Peng, *Nano Lett.*, 2016, **16**, 2133–2138.
- 36 S. Kubendhiran, Z. Bao, K. Dave and R.-S. Liu, *ACS Appl. Nano Mater.*, 2019, **2**, 1773–1790.
- 37 I. Lignos, R. Maceiczky and A. J. deMello, *Acc. Chem. Res.*, 2017, **50**, 1248–1257.
- 38 S. Duraiswamy and S. A. Khan, *Small*, 2009, **5**, 2828–2834.
- 39 A. Toyota, H. Nakamura, H. Ozono, K. Yamashita, M. Uehara and H. Maeda, *J. Phys. Chem. C*, 2010, **114**, 7527–7534.
- 40 Y. Roig, S. Marre, T. Cardinal and C. Aymonier, *Angew. Chem., Int. Ed.*, 2011, **50**, 12071–12074.
- 41 T. Gendrineau, S. Marre, M. Vaultier, M. Pucheault and C. Aymonier, *Angew. Chem., Int. Ed.*, 2012, **51**, 8525–8528.
- 42 J. Baek, Y. Shen, I. Lignos, M. G. Bawendi and K. F. Jensen, *Angew. Chem.*, 2018, **130**, 11081–11084.
- 43 A. Suea-Ngam, P. D. Howes, M. Srisa-Art and A. J. Demello, *Chem. Commun.*, 2019, **55**, 9895–9903.
- 44 T. W. Phillips, I. G. Lignos, R. M. Maceiczky, A. J. deMello and J. C. deMello, *Lab Chip*, 2014, **14**, 3172–3180.
- 45 R. M. Maceiczky, I. G. Lignos and A. J. deMello, *Curr. Opin. Chem. Eng.*, 2015, **8**, 29–35.
- 46 I. Lignos, V. Morad, Y. Shynkarenko, C. Bernasconi, R. M. Maceiczky, L. Protesescu, F. Bertolotti, S. Kumar, S. T. Ochsenbein, N. Masciocchi, A. Guagliardi, C.-J. Shih, M. I. Bodnarchuk, A. J. deMello and M. V. Kovalenko, *ACS Nano*, 2018, **12**, 5504–5517.
- 47 R. M. Maceiczky, K. Dömbgen, I. Lignos, L. Protesescu, M. V. Kovalenko and A. J. deMello, *Chem. Mater.*, 2017, **29**, 8433–8439.
- 48 L. Bezing, R. M. Maceiczky, I. Lignos, M. V. Kovalenko and A. J. deMello, *ACS Appl. Mater. Interfaces*, 2018, **10**, 18869–18878.
- 49 I. Lignos, L. Protesescu, D. B. Emiroglu, R. Maceiczky, S. Schneider, M. V. Kovalenko and A. J. deMello, *Nano Lett.*, 2018, **18**, 1246–1252.
- 50 I. Lignos, S. Stavrakis, G. Nedelcu, L. Protesescu, A. J. deMello and M. V. Kovalenko, *Nano Lett.*, 2016, **16**, 1869–1877.
- 51 I. Lignos, R. M. Maceiczky, M. V. Kovalenko and S. Stavrakis, *Chem. Mater.*, 2020, **32**, 27–37.
- 52 R. W. Epps, K. C. Felton, C. W. Coley and M. Abolhasani, *Lab Chip*, 2017, **17**, 4040–4047.
- 53 K. Abdel-Latif, R. W. Epps, C. B. Kerr, C. M. Papa, F. N. Castellano and M. Abolhasani, *Adv. Funct. Mater.*, 2019, **29**, 1900712.
- 54 I. Lignos, S. Stavrakis, G. Nedelcu, L. Protesescu, A. J. DeMello and M. V. Kovalenko, *Nano Lett.*, 2016, **16**, 1869–1877.



- 55 E. J. Braham, J. Cho, K. M. Forlano, D. F. Watson, R. Arróyave and S. Banerjee, *Chem. Mater.*, 2019, **31**, 3281–3292.
- 56 L. Wu, Q. Zhong, D. Yang, M. Chen, H. Hu, Q. Pan, H. Liu, M. Cao, Y. Xu, B. Sun and Q. Zhang, *Langmuir*, 2017, **33**, 12689–12696.
- 57 M. I. Bodnarchuk, S. C. Boehme, S. ten Brinck, C. Bernasconi, Y. Shynkarenko, F. Krieg, R. Widmer, B. Aeschlimann, D. Günther, M. V. Kovalenko and I. Infante, *ACS Energy Lett.*, 2019, **4**, 63–74.
- 58 Q. A. Akkerman, S. G. Motti, A. R. Srimath Kandada, E. Mosconi, V. D'Innocenzo, G. Bertoni, S. Marras, B. A. Kamino, L. Miranda, F. De Angelis, A. Petrozza, M. Prato and L. Manna, *J. Am. Chem. Soc.*, 2016, **138**, 1010–1016.
- 59 Z. Dang, J. Shamsi, F. Palazon, M. Imran, Q. A. Akkerman, S. Park, G. Bertoni, M. Prato, R. Brescia and L. Manna, *ACS Nano*, 2017, **11**, 2124–2132.
- 60 C. Wang, Y. Zhang, A. Wang, Q. Wang, H. Tang, W. Shen, Z. Li and Z. Deng, *Chem. Mater.*, 2017, **29**, 2157–2166.
- 61 Y. Bekenstein, B. A. Koscher, S. W. Eaton, P. Yang and A. P. Alivisatos, *J. Am. Chem. Soc.*, 2015, **137**, 16008–16011.
- 62 J. Cho, H. Jin, D. G. Sellers, D. F. Watson, D. H. Son and S. Banerjee, *J. Mater. Chem. C*, 2017, **5**, 8810–8818.
- 63 J. Cho, Y. H. Choi, T. E. O'Loughlin, L. De Jesus and S. Banerjee, *Chem. Mater.*, 2016, **28**, 6909–6916.
- 64 A. Ulman, *Chem. Rev.*, 1996, **96**, 1533–1554.
- 65 E. Fanizza, F. Cascella, D. Altamura, C. Giannini, A. Panniello, L. Triggiani, F. Panzarea, N. Depalo, R. Grisorio, G. P. Suranna, A. Agostiano, M. L. Curri and M. Striccoli, *Nano Res.*, 2019, **12**, 1155–1166.
- 66 T. Udayabhaskararao, L. Houben, H. Cohen, M. Menahem, I. Pinkas, L. Avram, T. Wolf, A. Teitelboim, M. Leskes, O. Yaffe, D. Oron and M. Kazes, *Chem. Mater.*, 2018, **30**, 84–93.
- 67 D. Zhang, S. W. Eaton, Y. Yu, L. Dou and P. Yang, *J. Am. Chem. Soc.*, 2015, **137**, 9230–9233.
- 68 J. Sui, J. Yan, D. Liu, K. Wang and G. Luo, *Small*, 2019, 1902828.
- 69 O. Voznyy, L. Levina, J. Z. Fan, M. Askerka, A. Jain, M.-J. Choi, O. Ouellette, P. Todorović, L. K. Sagar and E. H. Sargent, *ACS Nano*, 2019, **13**, 11122–11128.
- 70 B. Lambert, A. J. Gillen, N. Schuergers, S.-J. Wu and A. A. Boghossian, *Chem. Commun.*, 2019, **55**, 3239–3242.
- 71 R. Ramprasad, R. Batra, G. Pilania, A. Mannodi-Kanakkithodi and C. Kim, *npj Comput. Mater.*, 2017, **3**, 54.
- 72 K. T. Butler, D. W. Davies, H. Cartwright, O. Isayev and A. Walsh, *Nature*, 2018, **559**, 547–555.

